

# MICROSCOPIC INVESTIGATION OF FIELD EMITTERS LOCATED BY THERMOMETRY IN 1.5 GHz SUPERCONDUCTING NIOBIUM CAVITIES\*

JENS KNOBLOCH and HASAN PADAMSEE

*Laboratory of Nuclear Studies, Cornell University, Ithaca NY 14850, USA*

*(Received 11 January 1996; in final form 11 January 1996)*

A new high resolution, high speed thermometry system has been built to permit the study of field emitters in 1.5 GHz superconducting niobium cavities. Following a cavity test, the cavity is dissected for examination of the emitters in an electron microscope. Presented below is a survey of the topographical characteristics and composition of various defects found so far. A correlation between the current characteristics of emitters and their ability to process away was observed. It has been found that plasma production in the vicinity of an emitter is of importance in determining how much heat an emitter deposits on the rf surface as the electric field in the cavity is increased. In particular, this plasma plays a pivotal role in the extinction of emitters.

*Keyword:* Superconducting RF

## 1 INTRODUCTION

In present day niobium cavities the surface magnetic fields achieved still fall far short of those predicted by theory. The maximum field possible is believed to be the superheating rf field<sup>1</sup> (2300 Oe at 1.6 K). In practice, though, one finds that the cavity Quality ( $Q$ ) already begins to drop at fields between 300 and 1000 Oe. Most frequently the mechanism responsible for this anomalous power dissipation is field emission.<sup>2</sup> This may be so severe that the design field of a cavity cannot be attained because of power constraints or a field emission induced quench. In other cases, operational limits may be imposed due to bremsstrahlung produced by the emitted electrons. It is thus imperative to gain a better understanding of field emitters in rf cavities.

---

\*Supported by the National Science Foundation with supplementary support under the U.S.-Japan Agreement.

To this end a new thermometry system was developed which permits the study of emitters during cavity tests. Provided a cavity has interesting sites, it is subsequently cleanly cut into two half cells for examination in an electron microscope (SEM). An analysis of a site's composition with an energy dispersive X-ray analysis system (EDX) is also possible. By these methods we are able to study both active and inactive emitters.

The thrust of these experiments is to address three related questions:

- What is the mechanism responsible for the enhancement of field emission beyond the predictions<sup>3</sup> of the classic Fowler-Nordheim model?
- How do field emitters evolve on a microscopic scale as the cavity fields are increased?
- What is the mechanism responsible for the processing of field emitters, and can we predict at what field level an emitter will process?

The last of these questions is of practical importance. Knowledge of the processing mechanism may permit us to predict whether a cavity limited by emission can be salvaged by helium processing<sup>4</sup> or high peak power processing<sup>5</sup> rather than having to go through the laborious process of disassembly, cleaning and reassembly.

## 2 EXPERIMENTAL SETUP

Prior to testing, the cavities are dunked in nitric acid for an hour to remove any indium present from a previous test. This is followed by a chemical etch<sup>6</sup> in a 1:1:2 mixture of nitric, hydrofluoric and phosphoric acid (BCP) for a few minutes at temperatures below 18°C which removes about 3  $\mu\text{m}$  of niobium from the rf surface. Next the cavities are rinsed for at least two hours with deionized water in a continuous flow loop. The cavities are then dried with warm filtered nitrogen gas before being mounted on the test stand in a class 100 clean room.

To facilitate the search for field emitters, a new fixed thermometry system was built (Figure 1) whose details have been discussed elsewhere.<sup>7</sup> It is designed for 1.5 GHz single cell cavities operating in superfluid helium at 1.6 K in a vertical cryostat. Heating of the rf surface is detected by an array of 756 specially prepared carbon thermometers pressed against the outer cavity wall (Figure 2).

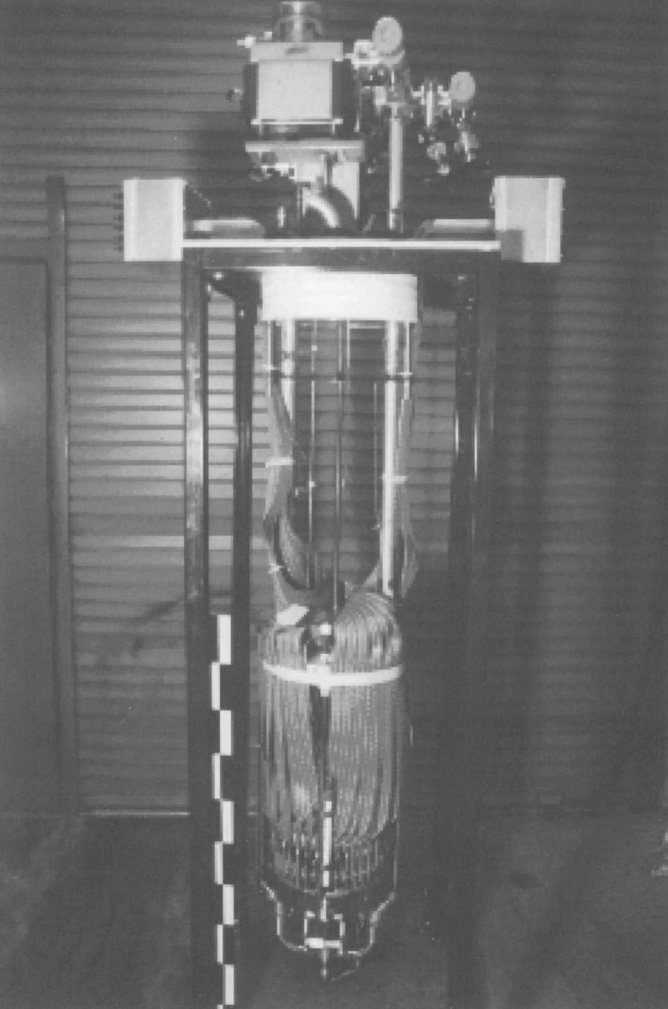


FIGURE 1 Test setup used for thermometry with 1.5 GHz cavities. The cavity and thermometers are hidden by the bottom end of the ribbon cables. Each thermometer has two wires leading out of the cryostat space through one of the rectangular feedthroughs visible above the top plate.

These sensors are cross calibrated with respect to a germanium thermometer during the initial cool down from 4.2 K to 1.6 K. By measuring the resistance of the thermometers using a four point technique their temperature rise above the bath's temperature can then be determined. A map at a resolution of 0.25 mK takes about 1/10 s to acquire. Increasing the acquisition time to 2.5 s permits us to resolve 30  $\mu$ K signals. In addition to this the computer used for the acquisition (a Macintosh) requires a few seconds to convert the measured resistances to temperatures. This is a marked improvement over previous systems which either were very slow, requiring several tens of minutes for an acquisition, or were unable to detect signals below 5 mK. Due to the short acquisition times we are able to track a cavity's temperature distribution as a function of applied field and are able to study several field emitters simultaneously.

Conventional rf power measurements<sup>8</sup> of the cavity  $Q$  versus peak electric ( $E_{pk}$ ) field were compared with results from calorimetry done with the thermometry system. Figure 3 illustrates that these results agree well, provided we calibrate the average thermometer sensitivity using one low field point of the conventional  $Q$  vs.  $E$  curve. Generally the thermometers register about 20% – 30% of the true temperature rise of the outside wall. This value varies somewhat from test to test due to differences in the cavities' surface characteristics and the thermometers' contact pressure.

In all tests the fields were increased to the maximum that could be attained with 50 W of rf power while monitoring the cavity temperature at intervals smaller than 1 MV/m. In one case, helium processing was successfully performed to stop emission from the dominant emitter.

After the tests, cavities that have interesting field emitters are cut apart. Two cuts are made with a regular pipe cutter across the beam tubes, 1.5 cm from the irises. A further cut is made with an oversized pipe cutter along the equator, as shown in Figure 4. During dissection the interior of the cavity is pressurized with filtered nitrogen gas in an effort to minimize dust contamination. The entire cutting process is carried out in a class 1000 clean room. The chamber of a commercial electron microscope has been enlarged to accommodate a complete half cell (Figure 5). By rotating the half cell about the beam axis and moving it along the  $y$ -axis of the SEM's stage we are able to examine most of the inside surface. In the past we have been able to show that thermometry data is a useful guide to locating emitters in the SEM.<sup>9</sup> A defect's composition can also be studied with an EDX system. The sensitivity of the EDX system is sufficient to detect foreign elements in particulates as small as 0.5  $\mu$ m

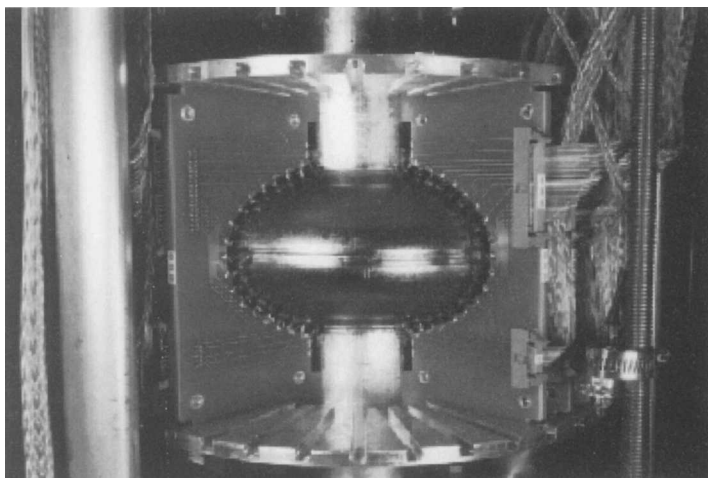


FIGURE 2 Close up view of the cavity with thermometers mounted. Several boards, holding 21 thermometers each, have been removed to expose the cavity. Altogether 756 thermometers are used.

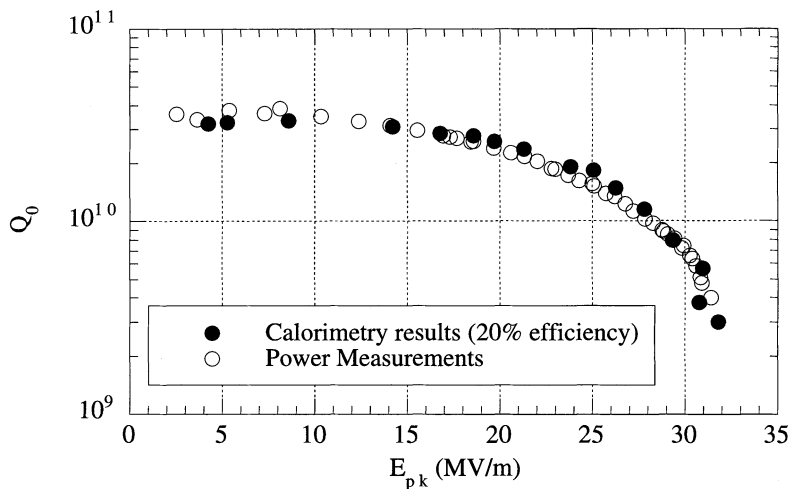


FIGURE 3 Comparison of the unloaded  $Q$  vs.  $E$  curves obtained ( $\bullet$ ) by calorimetry using the thermometry system, assuming a thermometer efficiency of 20% and ( $\circ$ ) by conventional power measurements.

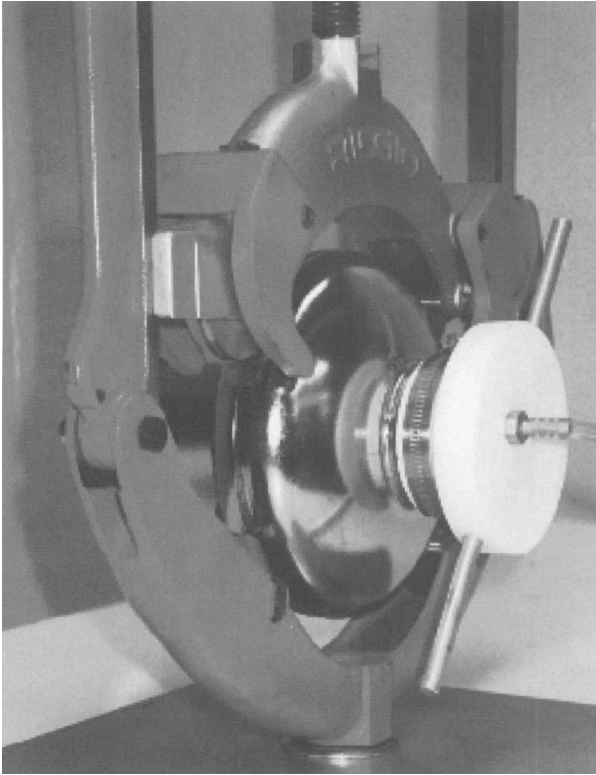


FIGURE 4 Illustration of a cavity being cut around the equator with a large pipe cutter following the removal of the beam tubes. The inside of the cavity is pressurized by filtered nitrogen gas through the tube at the front to minimize dust contamination on the inside. The rear end of the cavity is blanked off.

in size. On the other hand, we are able to see particles in the SEM which are 100 nm or larger.

The heating due to thermal defects (i.e. ohmic heating) occurs directly at the defect site. In contrast, field emitters are more difficult to pinpoint. Generally one detects the power deposited by accelerated field emission electrons impacting other parts of the cavity wall. For the  $TM_{010}$  mode that we use in the cavity tests, the trajectories are confined to the azimuth of the emission site and we detect a line of heating as shown in Figure 6.

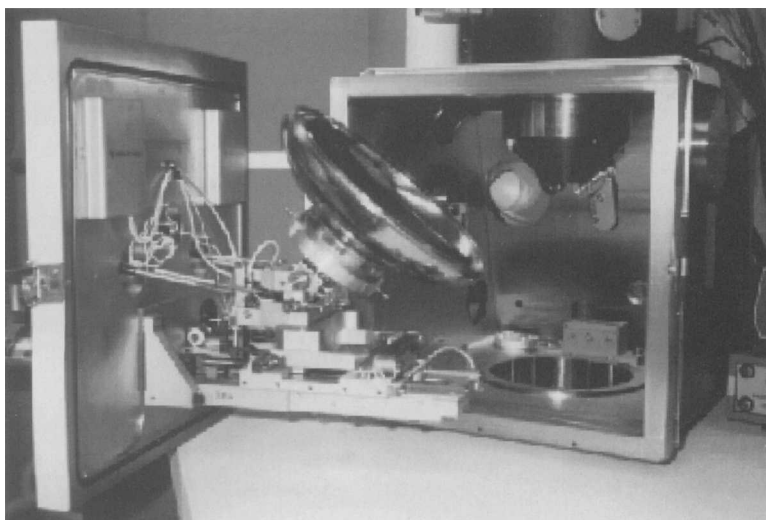


FIGURE 5 Photograph of the SEM chamber, slightly enlarged by the stainless collar to accommodate a half cell.

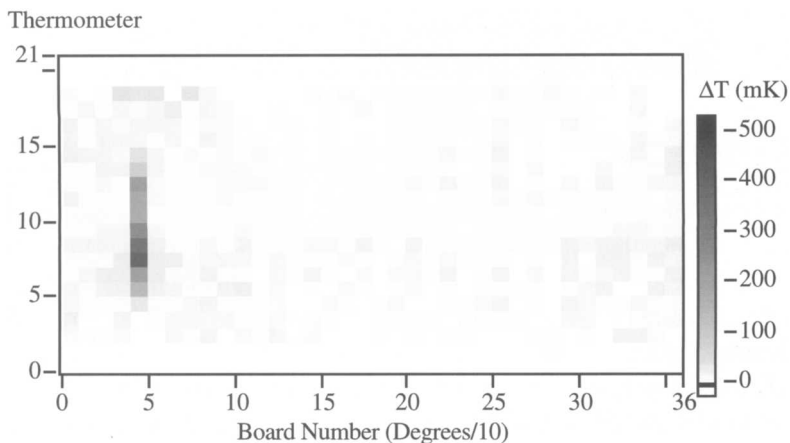


FIGURE 6 Typical temperature map illustrating the line heating detected due to field emitted electrons impacting with the cavity wall. The map is a flattened view of the cavity, with the horizontal representing the longitude around the cavity and the vertical representing the thermometer number at a given longitude.

To locate the actual emission site, we revert to trajectory calculations using the program MULTIP.<sup>9</sup> This computes the relativistic trajectories of electrons emitted at various phases of the rf cycle from a hypothetical emission site and tracks their motion until they collide with a cavity wall. The impact energies and current densities yield the power flux into the wall as a function of position. Thermal calculations permit us to determine the corresponding temperature rise at the outer-side of the cavity wall. By matching the calculated temperature distribution with the measured one we are generally able to determine the emitter location to within a few millimeters. This approach also has the benefit of yielding the field enhancement factor ( $\beta$ ) and the effective emission area used by the modified Fowler-Nordheim equation<sup>10,11</sup> to characterize the field emitter. The appropriate equation for niobium is<sup>2</sup>

$$I = 38.5 S \frac{(\beta E)^2}{t^2(y)} \exp\left(-54640 \frac{v(y)}{\beta E}\right) \quad (1)$$

where  $E$  is the electric field in MV/m,  $S$  is the effective emission area in  $\text{cm}^2$ ,  $y = 0.00948(\beta E)^{1/2}$  and  $v(y)$  and  $t(y)$  are functions given in various references.<sup>12</sup>

### 3 RESULTS AND DISCUSSION

#### 3.1 Field Emission Mechanism

Plotted in Figure 7 is the peak temperature rise of a field emitter that remained active at the maximum field attained during the test. At the predicted location we found jagged iron and chrome particles (presumably stainless steel) as shown in Figure 8.

Attempts to blow these particles away with a jet of  $\text{CO}_2$  'snow' failed, demonstrating that these particles had strongly adhered to the surface. The presence of jagged particulates at the emission location conforms well with the widely emerging view that metallic particulates are responsible for enhanced field emission. Among the various mechanisms proposed is the geometric enhancement of the applied electric field ("tip on tip model"<sup>13</sup>) which seems to hold true in this case.



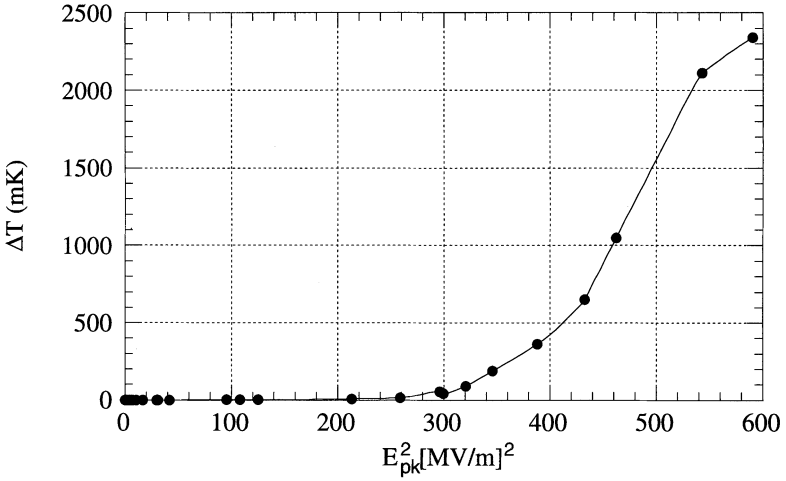


FIGURE 7 Peak temperature rise measured along the azimuth of the field emitter in Figure 8 illustrating that the emitter was still active at the end of the test.  $\Delta T$  is plotted versus  $E_{pk}^2$  to demonstrate the exponential departure of field emission heating from ohmic heating.

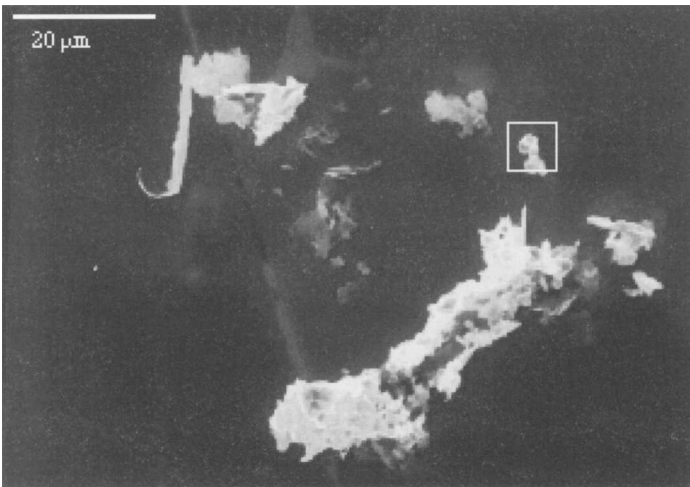


FIGURE 8 Depicted is the field emitter responsible for the heating in Figure 7. The main contaminants found at this site were iron and chrome. High pressure CO<sub>2</sub> ‘snow’ cleaning was unable to dislodge these particulates. The framed region is enlarged in Figure 11.

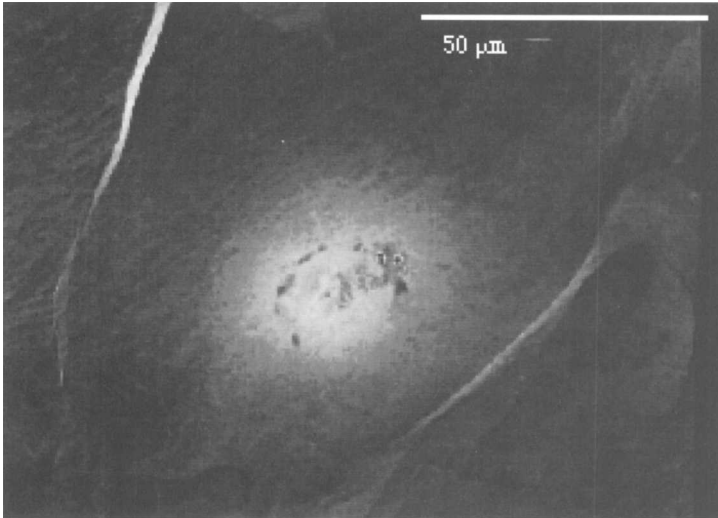


FIGURE 9 Picture of a field emitter active at the end of the test. The micron sized craters at 2 o'clock indicate the severity of the emission process. No foreign elements could be detected with an EDX system at this site and no particulates were found.

However, not all field emitters are the result of foreign particulates and geometric field enhancement. Another example of an emitter is depicted in Figure 9. Again, this site was emitting very strongly at the conclusion of the test, the peak temperature rise having been 450 mK at  $E_{pk} = 27.6$  MV/m. Yet, no particulates could be found at the emitter location. As experience with the previously described emitting particles showed, such particles tend to cling strongly to the rf surface. The lack of particulates in the case of Figure 9 thus implies that thin surface layers of adsorbed or chemically bound materials can enhance field emission without the necessity for particles.

Unfortunately, our EDX system is not sensitive enough to detect thin film residues. Previous studies<sup>14</sup> have shown that such thin films can be analyzed by the more sensitive Auger microscopy which we did not use to study this emitter.

Further evidence that geometric field enhancement is not the sole field emission mechanism can be seen in Figures 10(a) and (b). The former depicts the temperature map of a field emission free cavity at  $E_{pk} = 30.5$  MV/m. The sole hot spot on the equator is due to ohmic heating from a thermal defect.

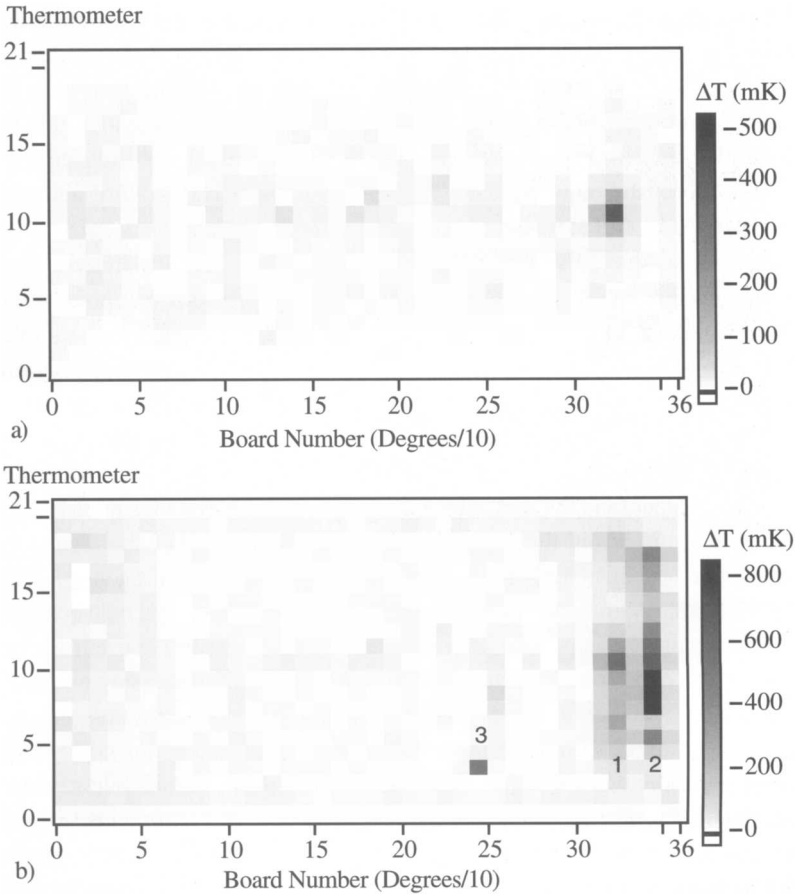


FIGURE 10 Maps taken at roughly  $E_{pk} = 30.5$  MV/m before and after the line heating due to two emitters (1 & 2) activated irreversibly. Site 3 did not display normal emission heating. The heating in (a) is quadratic in nature and not related to the field emitters in (b).

However, upon raising the input power the  $Q$  suddenly dropped and two field emitters (1 and 2 in Figure 10(b)) were activated simultaneously. Note the characteristic line heating associated with field emission. This activation process was irreversible but warming to room temperature deactivated emitter 2. It is difficult to explain such a simultaneous activation of two emitters using geometric field enhancement as the sole mechanism for enhanced field emission.

### 3.2 Evolution of Field Emitters

As frequently observed in the past, the current density drawn from a field emitter exceeds that required to melt the local environment.<sup>2,9</sup> This is shown to be true in Figure 11 which is a magnified view of the framed area in Figure 8. Similarly, some cratering is visible at the emission site in Figure 9, illustrating the severity of the emission process. Calculations<sup>2</sup> indicate that the current density required to melt niobium is about  $5 \times 10^{10}$  A/m<sup>2</sup> and this value was exceeded at both sites.

Past studies<sup>9</sup> have also shown that when the cavity fields are increased even further, the heating by the field emission current becomes severe enough that ultimately the emitter explodes and extinguishes ('processes'). An example of such a processed emitter is shown in Figure 12. A large dark region (starburst) surrounds the actual emission site which is marked by cratering, large scale melting and some debris. The main contaminant found among the debris was carbon. Auger studies in the past<sup>14</sup> have shown that the starburst region is cleaner than the rest of the cavity and it is believed that an extended plasma present during the explosion removes thin surface contaminants in the emitter's vicinity. DC studies carried out at Cornell<sup>2</sup> and Saclay<sup>15</sup> also confirmed that starbursts are created when arcing is initiated by a field emitter. Such plasmas, it was believed, were the result of the explosive event which destroys the emitter and thus are merely a side effect of processing events.

In view of this classic model of the behavior of particulate emitters and the evolution of these with increasing electric field, we were surprised to have found emitters as in Figure 13. This is, in fact, a low magnification image of the emitter depicted in Figure 9. Recall that this emitter remained active at the end of the cavity test. Note, though the presence of a starburst which implies that plasma activity actually plays a role during field emission prior to any ultimate processing event. Another example of the presence of a plasma prior to an emitter's explosion is shown in Figure 14. Again this emitter was active at the end of the test, yet we find a large starburst at the emission site. Zooming in on the center of this site, we find a sizable, previously molten region of titanium and carbon in addition to some small craters nearby.

The presence of a starburst before the processing of the emitter (Figures 13 and 14) establishes that a plasma can be present *during* the field emission stage. We now show that the occurrence of a large molten region also indicates that the plasma is responsible for additional heating of the rf surface. The field emission current alone cannot melt a 50  $\mu\text{m}$  region. This is shown by the following order of magnitude calculation.

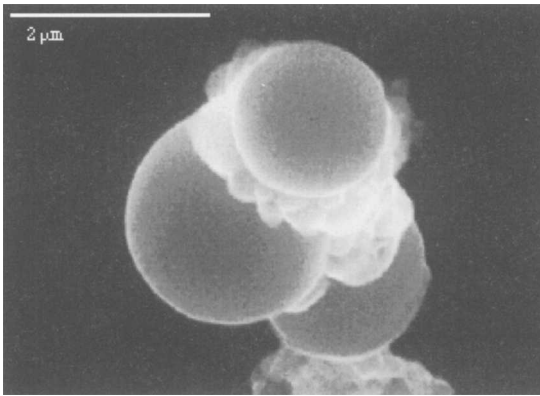


FIGURE 11 Enlarged view of the framed portion in Figure 8, clearly showing that parts of the stainless particulate had melted during the test.

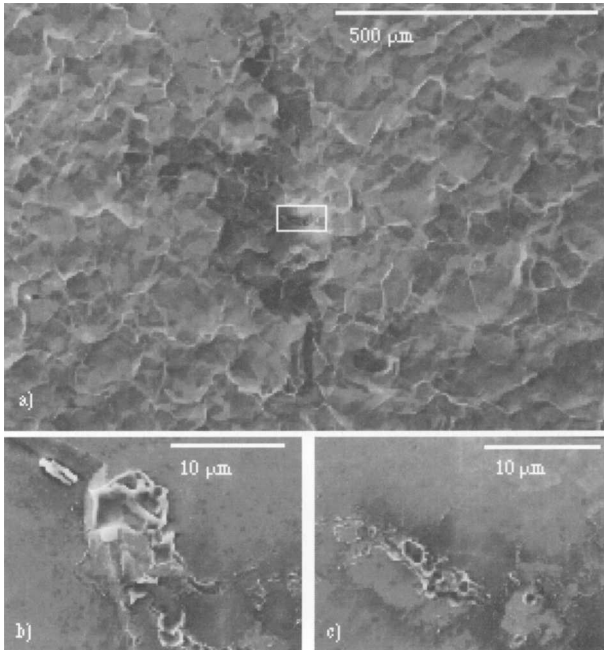


FIGURE 12 Shown is an emitter that was rf processed during the test. Images (b) and (c) are enlarged views of the central area, illustrating that large scale melting had occurred. Some debris is also visible, carbon being the main contaminant.

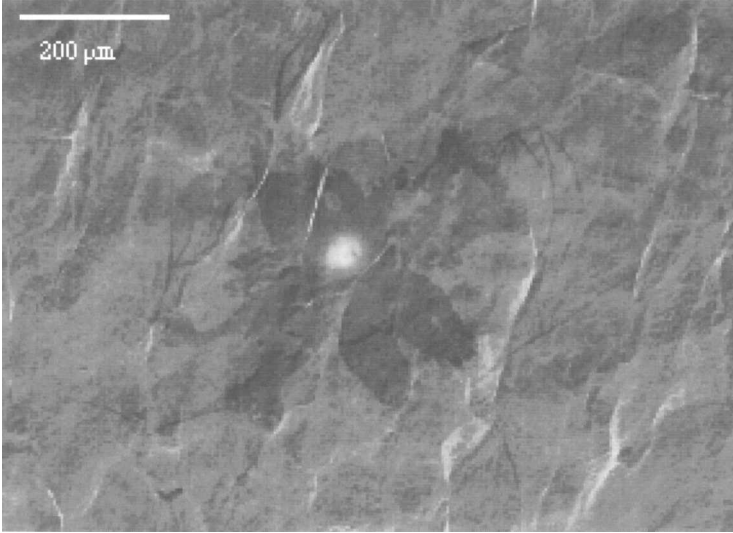


FIGURE 13 Low magnification photograph of the emitter in Figure 9 which was active at the end of the test. The starburst is indicative of plasma activity around the emitter despite the fact that the emitter did not process.

The total field emission currents we observe in cavities are typically no more than 1 mA. Given that normally the current densities are on the order of  $10^{11}$  A/m<sup>2</sup>, representative emission sites are not significantly larger than 0.1 μm across. Thus we treat an emitter as a point defect in the niobium surface. The power deposited by the emission current at the emitter site heats up the surface and the heat spreads in a hemisphere through the bulk of the cavity wall (Figure 15). Diffusion arguments yield the approximate radius of this expanding heat zone:

$$r(t) = \sqrt{Dt} \quad (2)$$

where  $D$  is the heat diffusion constant of the bulk.

The energy required to melt a unit volume of niobium<sup>2</sup> at 10 K is  $E_m = 10$  nJ/μm<sup>3</sup>. Hence the energy required to melt the entire heat zone is

$$E(t) = \frac{2}{3}\pi r^3 E_m = \frac{2}{3}\pi (Dt)^{3/2} E_m \quad (3)$$

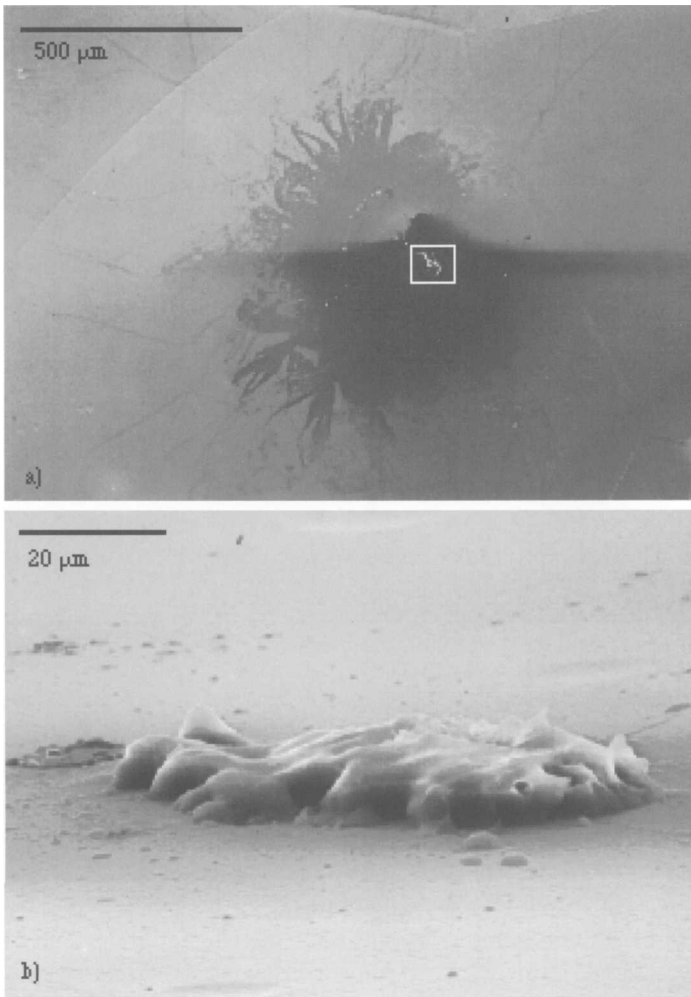


FIGURE 14 Photographs of an emitter active at the end of the test. The framed portion in (a) is enlarged in (b) and depicts a  $70\ \mu\text{m}$  large titanium and carbon particulate which had almost completely melted during the test. Note that (b) was taken at a near glancing angle with respect to the rf surface.

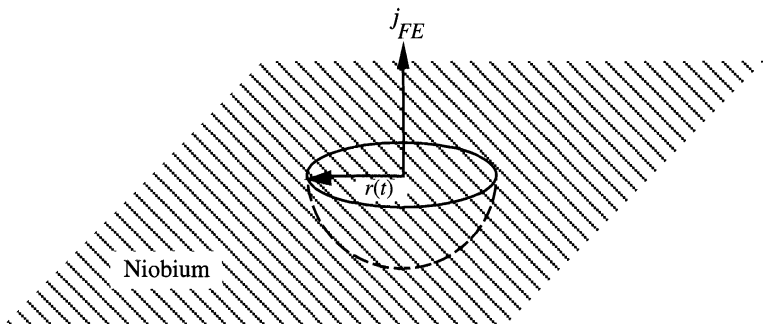


FIGURE 15 Geometry used to calculate the scale of melting due to the field emission current.

By differentiating with respect to time, we obtain the power required to continue melting the material through which the heat zone is expanding:

$$P(t) = \frac{dE}{dt} = \sqrt{t} \pi D^{3/2} E_m = \pi D r(t) E_m \quad (4)$$

Given that the field emission current dissipates a power  $P_{FE}$  we obtain the size of the molten region:

$$r(t) = \frac{P_{FE}}{\pi D E_m} \quad (5)$$

An upper limit for  $P_{FE}$  is about 0.1 W. We can set this limit because, with our thermometry system, we are unable to detect the heating at the emitter due to the field emitted current above the background heating produced by the impacting emission electrons. Ohmic dissipation greater than 0.1 W should result in a clear temperature signal above this background. Furthermore we know that the heat diffusion constant is roughly given by  $D = 1.5 \times 10^{-5} \text{ m}^2/\text{s}$ . The upper limit for the melt zone's size thus is

$$r_{\text{melt}} = 2 \times 10^{-7} \text{ m}$$

which is roughly in agreement with observed melting, as for example the craters in Figure 9.



If a field emitting particulate is not thermally anchored to the substrate, this calculation will not apply. However, in the cases we present here, where we find molten niobium it is unlikely that a  $50\ \mu\text{m}$  region of the niobium bulk can melt due to the field emission current alone.

The starbursts and the large molten regions show that a plasma must play an important role in melting areas larger than a few micrometers across. Such plasmas have been observed in DC field emission experiments.<sup>16–18</sup> Further evidence from previous cavity tests also substantiate this claim. For example, Figure 16 depicts a  $100\ \mu\text{m}$  starburst centered on small craters found in a 5.8 GHz cavity. At the periphery of the starburst we found molten stainless steel particulates. These particles are clearly too large to have originated from the craters, yet evidently had melted. The most obvious explanation is that the plasma responsible for the starburst also melted the particles.

To explain the source of this plasma in the absence of a processing event (spark) we need to modify our view of the field emission process. To this end we will refer to a region of enhanced field emission as a “macroemitter”. An example would be the stainless steel particle in Figure 8. It is reasonable to assume that the field emission enhancement ( $\beta$ ) varies locally and since field emission is exponential in field, a few small microemitters will dominate. This is illustrated in Figure 17. Once the current density exceeds a threshold of about  $5 \times 10^{10}\ \text{A/m}^2$ , individual microemitters will melt and may cease to emit. However, the overall emission characteristics of the macroemitter are only slightly changed. This would explain the observation that often emitters are a little unstable when the fields in the cavity are raised for the first time. (See for example Figure 7).

Due to the heating, neutrals outgas or desorb from the surface, leading to a buildup of a neutral gas in the vicinity of the emitter. At typical field levels in cavities (30 MV/m), emitted electrons will gain 30 eV within a micron of the rf surface and are then able to ionize the neutral gas. The ions in turn are accelerated by the fields towards the macroemitter and upon impact produce further heat and possibly secondary particles. This provides positive feedback for the evolution of neutrals and hence can lead to an avalanche situation. If individual microemitters explode, the neutral gas density is further enhanced and a starburst may be produced.

To be able to extinguish (process) the macroemitter we need to melt it completely. The power required to do this has to be supplied by the ions bombarding the rf surface, since the emission current alone is insufficient.

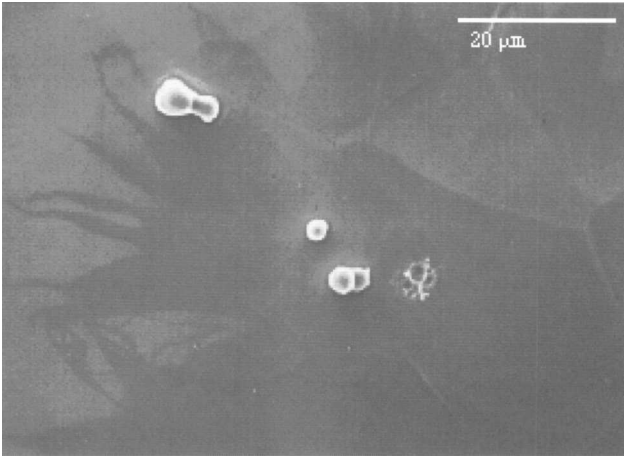


FIGURE 16 A field emitter found in a 5.8 GHz cavity. The previously molten iron particulate to the top left is too large to have been ejected by the craters and it is likely that it was melted by the same plasma that produced the starburst.

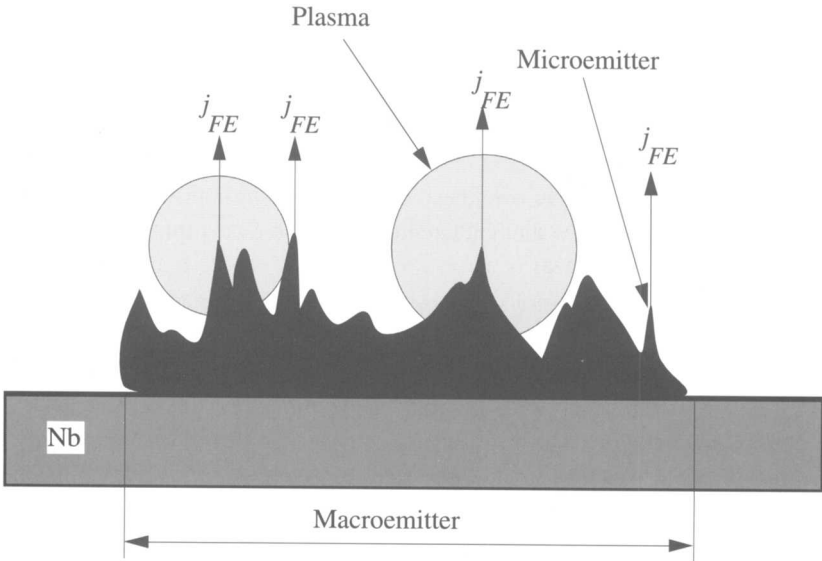


FIGURE 17 Schematic drawing illustrating a region of enhanced field emission (macroemitter) which is predominantly emitting from small areas within (microemitters). Due to the intense heating at the microemitters, neutrals are being desorbed and in turn are ionized by the emission current. It should be noted that, although in this figure the emission site is a particulate, this need not always be the case.

This bombardment rate is limited by the ionization rate of the neutral gas which in turn depends on a combination of the total current drawn from the macroemitter and the neutral gas density. Thus, to process an emitter, it is crucial that not only a current density threshold of at about  $5 \times 10^{10}$  A/m<sup>2</sup> is exceeded, but also a minimum total current needs to be emitted.

In the past, the observation that about  $10^{-4}$  torr of helium gas in the cavity helps to process emitters was addressed by a range of theories. In one explanation the helium is ionized by the field emission current and the ions gradually sputter the field emitter away.<sup>10,19</sup> Another theory is that helium ions are embedded in the emitter which results in a modification of the electronic structure and thus the field emission characteristics.<sup>20</sup>

In light of the important role that a plasma plays during field emission as outlined above, helium processing can easily be explained as well. Figure 18 depicts the  $Q$  v.  $E$  curves of a cavity before and after successful helium processing. This cavity was dominated by a single emitter (Figure 19(a)) which was completely extinguished after helium processing for less than one second (Figure 19(b)). At no time during helium processing did the fields in the cavity exceed those prior to the administration of helium when the emitter was stable. Upon examination of the cavity we again found a starburst (Figure 20(a)) centered on a previously molten region significantly larger than  $1 \mu\text{m}$  (Figure 20(b)). No foreign materials could be detected by EDX in this region. The melting must have occurred after the helium was administered to the cavity, otherwise it is likely that the emitter would have processed beforehand. Thus, prior to helium processing, the ion bombardment of the macroemitter was insufficient to melt it because either the neutral gas density or the current drawn was too low or both. The effect of the helium in this case is to artificially enhance the plasma density leading to premature processing.

The need to exceed a current density threshold as well as a current threshold to process an emitter is exemplified by the plot in Figure 21 which graphs the highest current drawn from various emitters versus the current density. The vertical line at  $5 \times 10^{10}$  A/m<sup>2</sup> represents an estimate of the current density threshold required to actually begin melting some microemitters. SEM examinations of emitters lying to the left of this line failed to turn up any sites that had clearly melted. The horizontal line at about 1 mA is an initial guess at the current threshold needed for processing. All field emitters that lie below this line were active at the conclusion of the cavity tests. There is only one emitter above this line and it did indeed process away in the

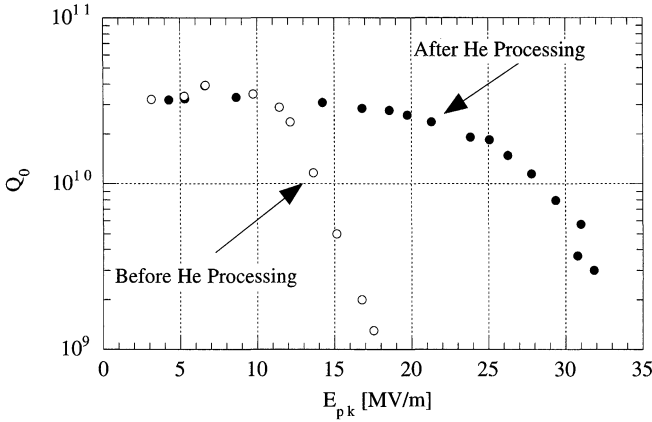


FIGURE 18  $Q_0$  v.  $E_{pk}$  curves obtained by conventional power measurements prior to and after helium processing. The low field  $Q$  remained unaffected whereas the field emission loading at high fields was drastically reduced by helium processing.

rf field. The helium processed emitter (marked by the asterisk) clearly lies in the middle of the unprocessed group.

A similar value for the processing current threshold was also observed during high peak power processing experiments.<sup>21</sup> Figure 22 plots the maximum current versus current density emitted by various sites, extrapolated to the fields achieved during the high peak power pulsing. Again we observe a current threshold of about 1 mA, above which all emitters processed.

One should note that ion bombardment of the emitter may not be the only effect the plasma has on the field emission process. The presence of the plasma near the emitter is bound to strongly perturb the electromagnetic fields in its vicinity. In particular it may enhance the local electric field. Since the emitted current increases exponentially with the electric field, small changes will affect the emission process very strongly. Again we are faced with a potential avalanche situation, once the total current exceeds the threshold required to produce a sufficiently dense plasma.

#### 4 CONCLUSION

Field emitters show a lot of variation in morphology and behavior and consequently it is difficult to extract a generic description from these

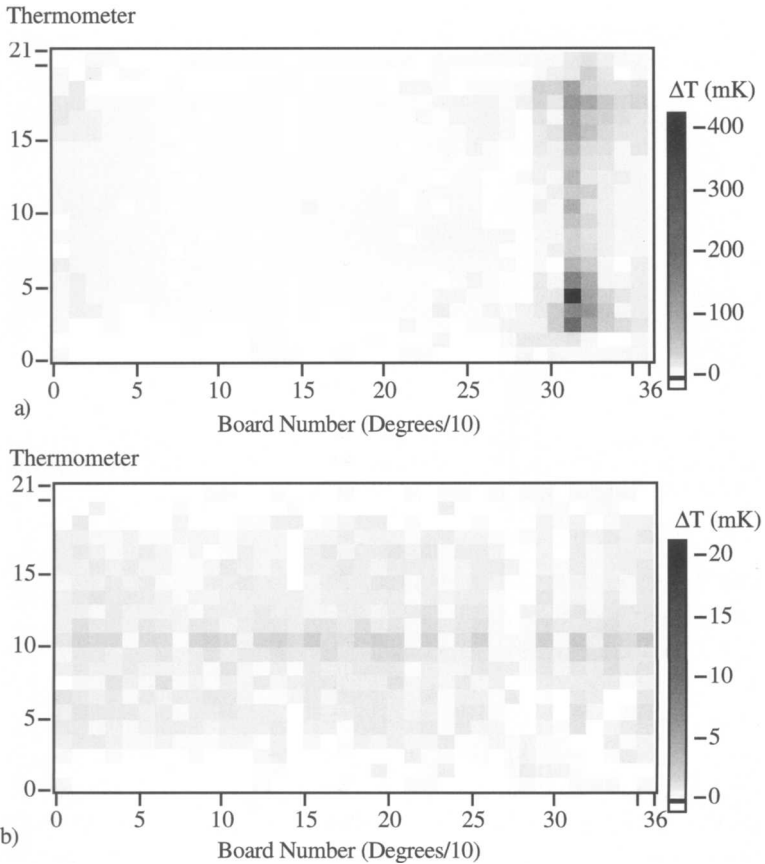


FIGURE 19 Temperature maps taken at  $E_{pk} = 17.3$  MV/m prior to (a) and after helium processing (b). The field emission related line heating visible in (a) is completely extinguished in (b). Note the drastic temperature scale change between the two maps.

experiments alone. However certain trends are observed which permit us to answer at least in part the questions posed in the introduction.

Many different mechanisms may be responsible for various emitters. Our results make it clear that enhanced field emission is not solely due to a geometric enhancement of the electric field. Other mechanisms which don't require particulates (larger than 100 nm) are also involved.

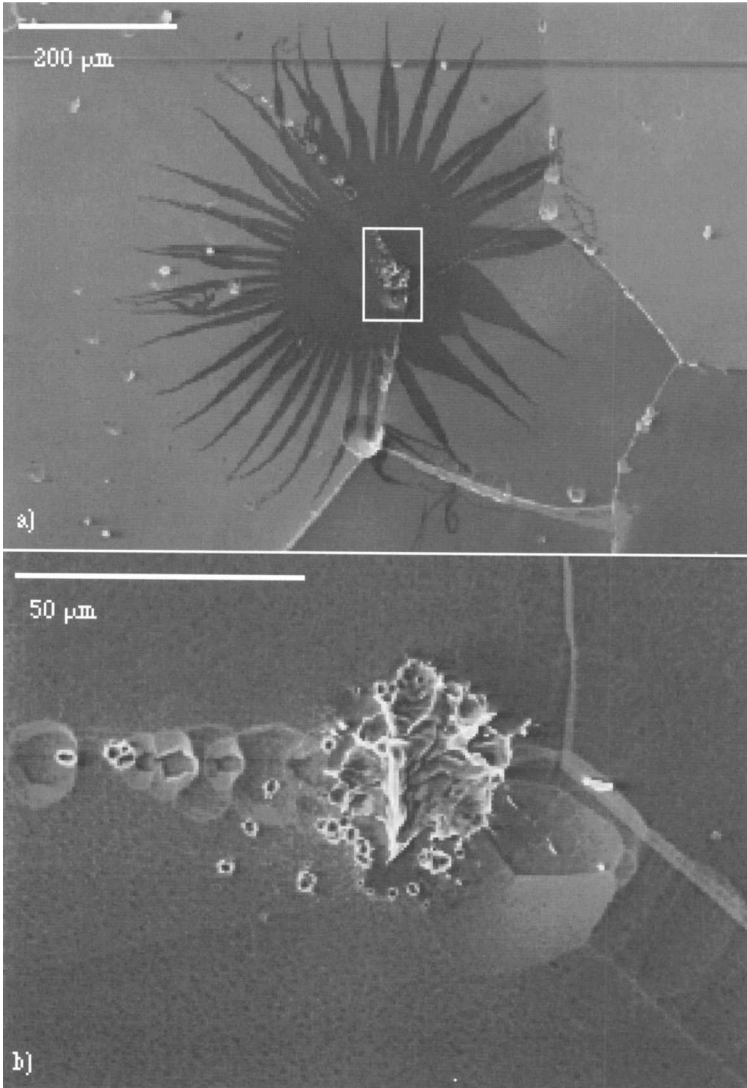


FIGURE 20 This emitter remained active at the highest field levels attained in the cavity ( $E_{pk} = 17.5$  MV/m) but then was successfully processed away after about  $10^{-4}$  torr of helium was administered to the cavity and fields again were raised to 17.5 MV/m. Note that the lower, enlarged picture is rotated counter-clockwise by about 60 degrees with respect to the upper one.

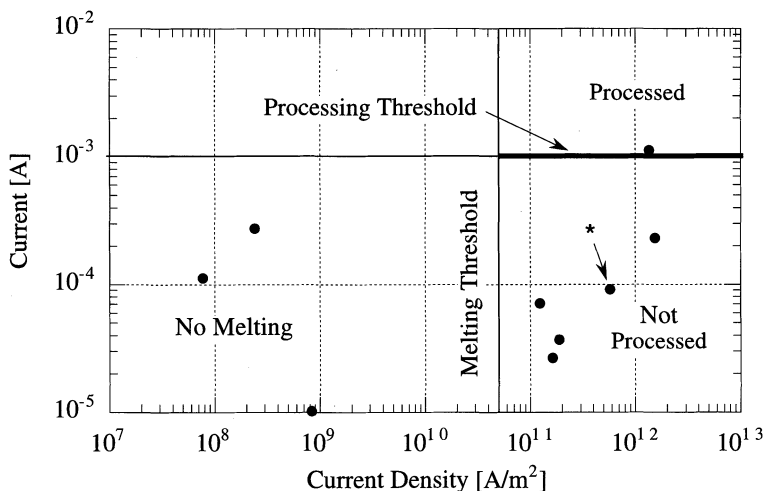


FIGURE 21 Maximum total current drawn versus current density for field emitters studied in cw mode in 1.5 GHz cavities. The emitter marked by the asterisk was later processed away with helium.

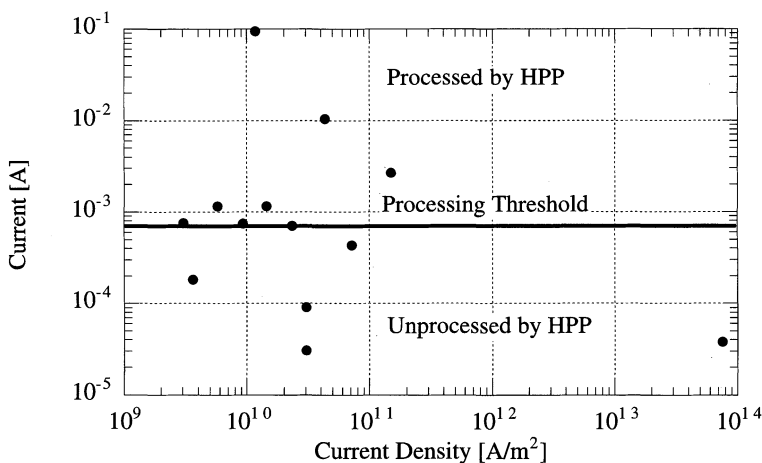


FIGURE 22 Maximum total current drawn versus current density for field emitters studied during high peak power processing in 3 GHz cavities. Note that the analysis yielding the current density was performed differently to that for Figure 21 and the current densities should all be multiplied roughly by a factor of 10 for comparison.

Initially a field emitter heats (and may melt) at microemitter sites. The extent of the heating is typically not larger than  $1 \mu\text{m}$  across. This results in the outgassing and desorption of neutrals which, in turn, are ionized by the emission current to produce a plasma. The plasma plays a pivotal role in heating the entire macroemitter and the consequent extinction of the emitter.

A field emitter will process once the emitted current density exceeds both the melting current density threshold and a total current threshold. Their values are likely to be in the  $5 \times 10^{10} \text{ A/m}^2$  and 1 mA ranges respectively, although these can vary significantly depending on differences in the composition and geometry of individual macroemitters.

## References

- [1] H. Piel, *CERN Accelerator School* (1988), 149.
- [2] D. Moffat, P. Barnes, T. Flynn, J. Graber, L. Hand, W. Hartung, T. Hays, J. Kirchgessner, J. Knobloch, R. Noer, H. Padamsee, D. Rubin and J. Sears, *Particle Accelerators*, **40** (1992), 85.
- [3] R.H. Fowler and L. Nordheim, *Proc. Roy. Soc. Lond.*, **A119** (1928), 173.
- [4] H. Padamsee, *AIP Conf. Proc.*, **249** (1990), 1403.
- [5] J. Graber, C. Crawford, J. Kirchgessner, H. Padamsee, D. Rubin and P. Schmüser, *Nucl. Instr. and Meth. in Phys. A*, **350** (1994), 572.
- [6] P. Kneisel, *Proc. of the Workshop on rf Superconductivity*, Karlsruhe (1980), 275.
- [7] J. Knobloch, H. Muller and H. Padamsee, *Rev. Sci. Instrum.*, **65** (11) (1994), 3521.
- [8] J. Knobloch, SRF Group, Cornell University, internal SRF note 910927-07, unpublished.
- [9] J. Graber, J. Kirchgessner, D. Moffat, J. Knobloch, H. Padamsee and D. Rubin, *ibid.*, **5** 582.
- [10] H.A. Schwettman, J.P. Turneaure and R.F. Waites, *J. Appl. Phys.*, **45**(2) (1974), 914.
- [11] R.J. Noer, *Appl. Phys A*, **28** (1982), 1.
- [12] E.L. Murphy and R.H. Good, Jr., *Phys. Rev.*, **102** (6) (1956), 1464.
- [13] M. Jimenez, R.J. Noer, G. Jouve, J. Jodet and B. Bonin, *J. Phys. D*, **27** (1994), 1038.
- [14] T. Hays, S. Durbin, M. Gray, M. Klauda, J. Knobloch, D. Moffat and H. Padamsee, *Proc. of the 6th Workshop on RF Superconductivity*, CEBAF (1993), 750.
- [15] R.J. Noer, *ibid.*, 236.
- [16] B. Jüttner, *Nuclear Instruments and Methods in Physics Research*, **A268** (1988), 390.
- [17] S.P. Bugaev, A.M. Iskol'dskii, G.A. Mesyats and D.I. Proskurovskii, *Soviet Physics—Technical Physics*, **12** (12) (1968), 1625.
- [18] G.A. Mesyats and D.I. Proskurovsky, *Pulsed Electrical Discharge in Vacuum*, Springer Verlag (1989).
- [19] D. Alpert, D.A. Lee, E.M. Lyman and H.E. Tomaschke, *J. Appl. Phys.*, **38** (1967), 880.
- [20] S. Bajic and R.V. Latham, *IEEE Trans. Elec. Insul.*, **23** (1) (1988), 8.
- [21] J. Graber, Ph.D. Thesis, Cornell University (1993).